Comptes Rendus

Géoscience

Sciences de la Planète

Catalina Morales-Yáñez, Zacharie Duputel and Luis Rivera

Exploring the link between large earthquakes and magma transport at the onset of the Mayotte volcano-seismic crisis

Part of Special Issue: The Mayotte seismo-volcanic crisis of 2018-2021 in the Comoros archipelago (Mozambique channel)

Guest editors: Jérôme Van der Woerd (Institut Terre Environnement de Strabourg, UMR 7063 CNRS / Université de Strasbourg, 67084 Strasbourg, France), Vincent Famin (Laboratoire Géosciences Réunion, Université de La Réunion - IPGP, 97744 Saint-Denis, France) and Eric Humler (Professeur Université de Nantes, Laboratoire de Planétologie et Géosciences, UMR 6112, Faculté des Sciences et Techniques, Nantes Université, 44322 Nante, France)

The Mayotte seismo-volcanic crisis of 2018-2021 in the Comoros archipelago (Mozambique channel) / *La crise sismo-volcanique de 2018-2021 de Mayotte dans l'archipel des Comores (Canal du Mozambique)*

Exploring the link between large earthquakes and magma transport at the onset of the Mayotte volcano-seismic crisis

Catalina Morales-Yáñez [*, a, b]**, Zacharie Duputel** [c, d] **and Luis Rivera** [a]

[a] Institut Terre et Environnement de Strasbourg, UMR7063, Université de Strasbourg/EOST, CNRS, Strasbourg, France

[b] Department of Civil Engineering, Universidad Católica de la Santísima Concepción, Concepción, Chile

[c] Observatoire Volcanologique du Piton de la Fournaise, Université de Paris, Institut de Physique du Globe de Paris, CNRS, F-75005, Paris, France

[d] Université de Paris, Institut de physique du globe de Paris, CNRS, F-75005 Paris, France

E-mails: catalina.morales@ucsc.cl (C. Morales-Yáñez), duputel@ipgp.fr (Z. Duputel), luis.rivera@unistra.fr (L. Rivera)

Abstract. The archipelago of Comoros was generally considered a moderately seismic region. However, since May 2018, unusual seismicity has been observed off the east coast of Mayotte Island. Following this increase of seismic activity, oceanographic campaigns led to the discovery of a new submarine volcano, indicating that the observed seismicity had a volcanic origin. In this study, we estimate Centroid Moment Tensor (CMT) solutions of $M_w \geq 5$ earthquakes of this sequence using 3D Green's functions and analyze their non-double-couple (non-DC) components. Consistently with previous reports, our results indicate that seismicity migrated upward in May–June 2018 with an increasing number of non-DC events. We show that non-DC components observed in our solutions and previously published catalogs cannot correspond to dike opening or closing as the observed rupture durations suggest unrealistically large magma flow rates. Given that waveforms can be relatively well explained with pure-shear sources, we postulate that non-DC components are most likely artifacts due to unmodeled shallow structural heterogeneities. Most $M_w \geq 5$ earthquakes have a strike-slip mechanism consistent with the rupture of pre-existing faults loaded by the regional stress regime and triggered by the increment of stress produced by the upward magma transfer.

Keywords. Mayotte, Volcano seismology, Moment tensor inversion, 3D-Green functions, Volcano-tectonic earthquakes.

Published online: 21 October 2022, Issue date: 17 January 2023

---

* Corresponding author.

1. Introduction

Mayotte Island is one of the four islands of the Comoros volcanic archipelago. It is located in the Indian Ocean in the Mozambique Channel between Madagascar and Africa. Mayotte Island shows marked volcanic geomorphology. Volcanism in Mayotte started about 10 to 15 My ago [Audru et al., 2010]. This behavior continued during the Quaternary, with the last volcanic eruption occurring 7000 years ago [Zinke et al., 2003]. The source of volcanic activity in Mayotte is still debated. Emerick and Duncan [1982] suggests that the origin of the archipelago is a hotspot, while Nougier et al. [1983] postulates that the volcanism corresponds to the reactivation of old and deep lithospheric fractures. Michon [2016] also rejects the idea of a hotspot and proposes that the Comoros archipelago volcanic activity can be explained by lithospheric deformation related to the southern extension of the East-African rift.

In general, the archipelago of Comoros is considered a moderately seismic region. However, since May 10, 2018, unusual intense seismicity has been observed in the east of Mayotte Island. From May 10, 2018 to July 31, 2019 almost 2000 events with local magnitude $M_L \geq 3.5$, were recorded [REVOSIMA/IPGP, 2019]. The largest earthquake occurred on May 15, 2018, with a magnitude of $M_w = 5.9$. After July 2018, the number of earthquakes decreased, showing less than a hundred earthquakes with magnitude $M_L \geq 3.5$ per month [REVOSIMA/IPGP, 2019, Saurel et al., 2022]. Although the most significant earthquakes occurred at the beginning of the crisis, the region remains active in 2021 with 141 $M_W \geq 1$ Volcano-Tectonic (VT) earthquakes located in December 2021 [REVOSIMA/IPGP, 2021]. Geodetic data recorded in Mayotte show transient displacements of approximately 17–20 cm to the east and subsidence of 8 to 15 cm from the beginning of the crisis until the end of July 2019 [Figures 5 and 6 of the Bulletin number 1; REVOSIMA/IPGP, 2019]. Very long-period events (VLP) with a dominant period of ~15 s have also been reported [Cesca et al., 2020, Lemoine et al., 2020]. An oceanographic campaign in the area led to the discovery of a new submarine volcano in May 2019, located approximately 50 km east of Mayotte, which forms a seamount of approximately 820 m height on the seafloor [Feuillet, 2019]. This campaign and later oceanographic campaigns have revealed several lava flows along with acoustic plumes in the water column. The new volcano is located at the tip of a 50-km-long ridge composed of many recent volcanic edifices, interpreted as an extensional structure within an east–west striking zone between East Africa and Madagascar [Feuillet et al., 2021, Famin et al., 2020]. Assuming that the new volcano edifice began to be built in July 2018, the mean lava flow rate is approximately 180 m$^3 \cdot$s^{-1} (according to a survey conducted 11 months after onset of eruption [Feuillet et al., 2021]). The extruded volume of lava could be as large as 5 km^3 transforming it into the largest active submarine eruption ever documented [Feuillet et al., 2021].

Following the deployment of additional seismological stations both onland and offshore, two separate seismicity clusters are now identified [Saurel et al., 2022]. Most of the large $M_W \geq 5.0$ earthquakes that occurred at the beginning of the crisis were located in a distal cluster connecting deep parts of the plumbing system (at depth of 30–40 km) to the new volcanic edifice on the seafloor [Cesca et al., 2020, Feuillet et al., 2021, Saurel et al., 2022]. This initial seismic sequence was most likely associated with the migration of magma toward the surface. Later, the magnitude of earthquakes decreased progressively and the seismic activity migrated toward Mayotte island. This proximal cluster, located 10 km to the east of Mayotte, has a cylindrical shape that likely corresponds to a ring fault system below an ancient caldera structure [Feuillet et al., 2021].

In this study, we analyze the source of the VT earthquakes to constrain the spatio-temporal properties of magma migration at the onset of Mayotte volcano-seismic activity. The unusual increase of earthquake activity along with the birth of the large volcanic edifice offshore of Mayotte clearly indicate the magmatic origin of the seismic sequence. However, the relationship between the observed large ($M_w \geq 5.0$) earthquakes and the migrating magma pressure source is still elusive. In particular, several VT events in Global CMT [GCMT, Dziewonski et al., 1981, Ekström et al., 2012] and Cesca et al. [2020] catalogs present large non-double-couple (non-DC) components. These non-DC events could potentially correspond to volcanic source processes such as dike opening due to magma migration, resonance of fluid-filled cracks or even complex ruptures on ring-faults [Ekström, 1994, Chouet and Matoza, 2013,

Rodríguez-Cardozo et al., 2021]. These non-DC components could also be associated with complex ruptures involving multiple tectonic subfaults or have a spurious origin and be induced by measurement errors (e.g., noise) or modeling uncertainties (e.g., inaccuracy of the Earth model). Here we focus on trying to understand to what extent these earthquakes correspond to opening/closing dykes or whether they correspond to shear faulting caused by stress transfer caused by a migrating magmatic pressure source.

With this purpose, we use long-period waveforms to invert for the source parameters of $M_w \geq 5$ earthquakes that essentially occurred during the first months of the Mayotte seismic crisis (May and June 2018). Unfortunately, few regional stations were available during this period. Hence, the inversion is based on long-period seismological observations, including body and surface waves. To mitigate the impact of lateral heterogeneities that can be particularly large for fundamental mode surface waves, we estimate the Centroid Moment Tensor (CMT) parameters using Green's functions computed for a global 3D Earth model combining S40RTS and CRUST2.0 [Ritsema et al., 2011, Bassin et al., 2000]. We compare our solutions with other studies and discuss the magma transfer at the beginning of the seismo-volcanic crisis.

2. Data and methods

We select events from the GCMT catalog located in the vicinity of Mayotte Island in 2018. This selection gives a total of 27 events with $M_w \geq 4.8$, occurring mostly at the beginning of the crisis (i.e. in May–June 2018). We use teleseismic and regional waveforms from stations with an epicentral distance from 0° to 90°. We use a combination of 150 channels from GEOFON [IS, GE, TT; GEOFON Data Centre, 1993], GEOSCOPE [G; Institut de Physique du Globe de Paris (IPGP) and Ecole et Observatoire des Sciences de la Terre de Strasbourg (EOST), 1982], ASL/USGS [AU, IU, IC, GT; Albuquerque Seismological Laboratory (ASL)/USGS, 1988, 1992, 1993], IRIS/IDA [II; Scripps Institution of Oceanography, 1986], MedNet [MN; MedNet Project Partner Institutions, 1990], RE-SIF [FR, RD; RESIF, 1962, 2018], NARS [NR; Utrecht University (UU Netherlands), 1983], Karthala [KA; Institut de Physique du Globe de Paris (IPGP), 2006] as well as station GULU belonging to a temporary

network installed in Uganda to investigate plume-lithosphere interactions [XW; Nyblade, 2017]. Waveform data has been validated at long period by comparing with synthetics from large teleseismic earthquakes. We do not use the YTMZ strong motion station from the French RESIF-RAP network, which was the only station on Mayotte Island at the beginning, due to large errors in the internal clock during the studied time-period.

For each earthquake, we manually reject noisy records and data with dubious metadata. After data screening, moment tensor solutions are obtained using 23 channels in average. The time window used for the waveform inversion starts at the P-wave arrival and includes the first group of surface waves (R1 and L1). For specific stations, we manually change the time window duration to exclude clipped signals in the inversion. A causal bandpass Butterworth filter of order 4 is applied to the data. To mitigate long-period seismic noise, the filter corner periods are adapted as a function of the earthquake magnitude and the epicentral distance of the stations (see Tables 1 and 2). Using the resulting long-period waveforms, we then perform point source inversions to invert for CMT parameters (i.e., moment tensor elements, rupture duration, and centroid location in time and space). We use a modified version of the W-phase inversion method by Duputel and Rivera [2019]. This algorithm relies on a grid-search approach to find the point-source mechanism, time and location that minimizes the root mean square (RMS) waveform misfit. In this study, we assume three different levels of generality for the moment tensor: (1) Full moment tensor (FMT; i.e., six independent elements of the symmetric moment tensor), (2) Deviatoric moment tensor (DMT; i.e., assuming no net volume change during the rupture) and (3) Double-Couple (DC; i.e., assuming a pure shear rupture). While FMT and DMT inversions are linear for a given centroid location, DC solutions are estimated by grid-searching for strike, dip and rake angles corresponding to the minimum RMS misfit. For the sake of consistency, FMT and DC inversions are performed using the same dataset, time shift (T_s) and centroid location as those estimated for the DMT solution.

To account for large-scale 3D heterogeneities, we compute Green's functions using SPECFEM3D_GLOBE [Komatitsch et al., 2015] for a global 3D Earth model composed of S40RTS

Table 1. Bandpass filter used for records with epicentral distance larger than 4°

Magnitude	Bandpass
$5.3 \leq M_w \leq 5.9$	50–150 s
$M_w < 5.3$	50–100 s

With the exception of earthquakes 2018-06-04 21:20, $M_w = 5.1$ and 2018-06-01 07:14, $M_w = 4.7$ for which we use 50–150 s and 30–80 s passbands respectively.

Table 2. List of events for which an ad-hoc bandpass filter is applied for stations at epicentral distances smaller than 4°

Event	Magnitude	Bandpass
2018-05-15 15:48	5.9	50–150 s
2018-06-12 17:17	5.4	50–150 s
2018-06-25 17:41	5.3	50–150 s
2018-06-27 06:40	5.2	50–100 s
2018-06-18 13:43	5.1	50–100 s
2018-06-23 19:45	5.0	50–100 s
2018-06-05 23:02	5.1	30–80 s
2018-05-30 05:54	5.1	30–80 s
2018-05-25 09:32	5.0	30–80 s
2018-06-07 13:06	5.0	30–50 s
2018-06-10 13:04	4.8	30–50 s

[Ritsema et al., 2011] and CRUST2.0 [Bassin et al., 2000]. Green's functions are calculated for various source locations with depth ranging from 5.0 to 35.0 km (each 2.5 km), latitude ranging from 13.03° S to 12.7° S and longitudes ranging from 45.48° E to 45.83° E (each 0.025°). The definition of this grid was guided by the earthquake centroid locations provided by the GCMT catalog and preliminary tests.

Once we obtain the moment tensor parameters we perform a decomposition of the moment into the double couple (DC), isotropic (ISO), and compensated linear vector dipole (CLVD). For this, we follow the definition of Vavryčuk [2015],

$$M_{\text{ISO}} = \tfrac{1}{3}(M_1 + M_2 + M_3) \tag{1}$$

$$M_{\text{CLVD}} = \tfrac{2}{3}(M_1 + M_3 - 2M_2) \tag{2}$$

$$M_{\text{DC}} = \tfrac{1}{2}(M_1 - M_3 - |M_1 + M_3 - 2M_2|)$$
$$(M_{\text{DC}} \geq 0) \tag{3}$$

where, $M_1 \geq M_2 \geq M_3$ correspond to the eigenvalues of the moment tensor. Then to measure the relative contribution of each component, we can write,

$$\begin{bmatrix} C_{\text{ISO}} \\ C_{\text{CLVD}} \\ C_{\text{DC}} \end{bmatrix} = \frac{1}{M} \begin{bmatrix} M_{\text{ISO}} \\ M_{\text{CLVD}} \\ M_{\text{DC}} \end{bmatrix} \tag{4}$$

where $M = |M_{\text{ISO}}| + |M_{\text{CLVD}}| + M_{\text{DC}}$ and $|C_{\text{ISO}}| + |C_{\text{CLVD}}| + C_{\text{DC}} = 1$. This relation allows to define the contribution of each component.

3. Earthquake migration uncovering a deep magma transfer in May–June 2018

The spatio-temporal distribution of earthquakes after CMT inversion is shown in Figure 1. Events are roughly aligned along a NW–SE structure with deeper earthquakes at the NW and shallower events at the SE (Figure 1a). Although our centroid locations are globally consistent with other catalogs (see comparison with GCMT and Cesca et al. [2020] in Supplementary Figure 1), there are some differences that result from the use of different Earth models, frequency bands and choice of seismological stations. For example, Cesca et al. [2020] use 1D velocity models and includes the local strong-motion station YTMZ (mitigating clock drifting issues by inverting for time-shifts at each station). In contrast, our study is based on a 3D global velocity model and does not include YTMZ. As shown in Figure 1b, the seismic events migrate upward along this NW–SE structure from a depth of ~35 km toward the surface between mid-May and early June 2018. This seismicity migration is a robust feature that is clearly visible in multiple catalogs (GCMT, Cesca et al. [2020] and Lemoine et al. [2020]; cf., Supplementary Figure 1). These migrating earthquakes have been interpreted as the markers of a deep magma transfer at the origin of the new volcano evidenced by Feuillet [2019]. Magma likely originated from one or multiple reservoirs or mushes located at depth ranging from 25 and 60 km depending on the estimates [Lemoine et al., 2020, Cesca et al., 2020, Feuillet et al., 2021]. The absolute centroid depth of earthquakes might depends on the assumed local velocity structure, which is poorly known in the vicinity of Mayotte [Cesca et al., 2020, Dofal et al., 2021].

Earthquake migration associated with magma transfer has been observed in many volcanic areas
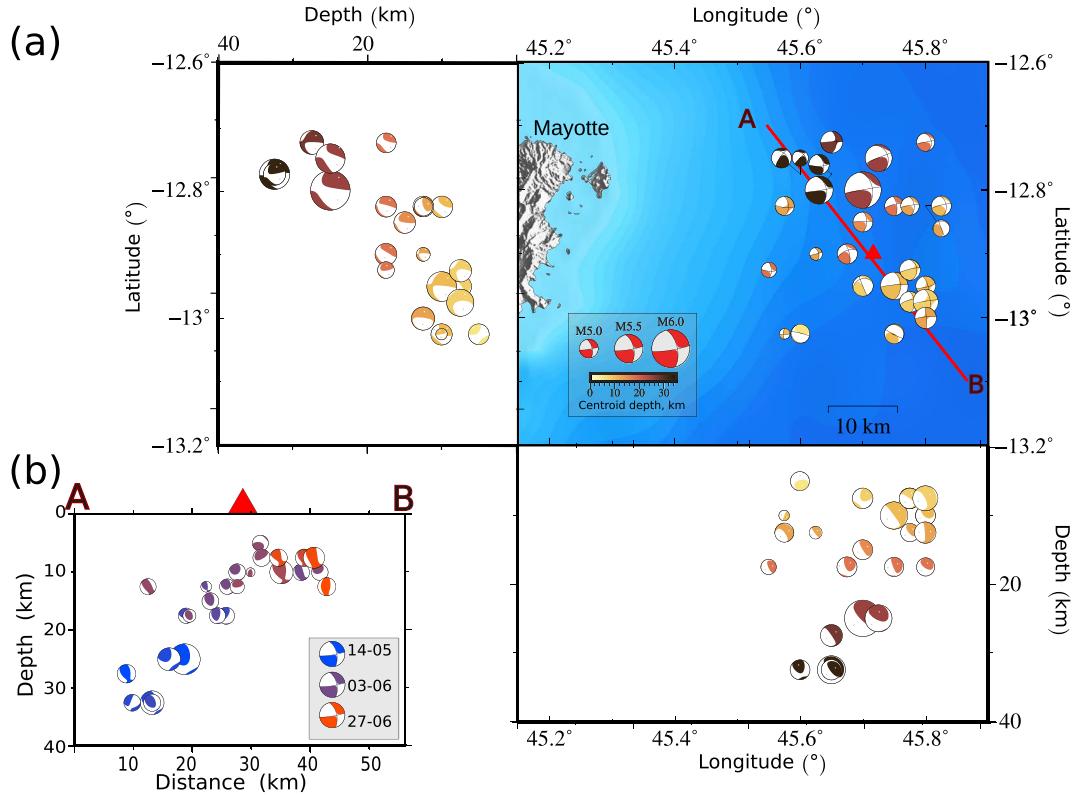
Figure 1. Spatial distribution of moment tensor solutions for the deviatoric inversion. (a) The (lower hemisphere) beachballs are positioned on the map at the estimated centroid locations. Colors correspond to the centroid depth. The red triangle indicates the position of the volcano [REVOSIMA/IPGP, 2019]. The two side panels are NS and EW vertical cross sections including beachball visualized from the W and S respectively (back hemisphere beachballs). (b) Vertical A–B cross section. Back hemisphere beachballs (visualized from the SW) are colored according to the event date. Color scale starts on May 14, 2018 (red) and ends on June 27, 2018 (blue). The position of the volcano at the free surface is indicated with a red triangle.

such as the Bároarbunga volcanic system in Iceland [Sigmundsson et al., 2015, Ágústsdóttir et al., 2016], the Kilauea volcanoes in Hawaii [Neal et al., 2019, Lengliné et al., 2021] and the Piton de la Fournaise volcano in La Réunion [Battaglia et al., 2005, Lengliné et al., 2016, Duputel et al., 2019]. However, as noted by Cesca et al. [2020] and Feuillet et al. [2021], deep crustal earthquakes associated with deep magma transfer is less common. Such seismicity at depths larger than 10 km has been previously observed at Lo'ihi and Kilauea volcanoes in Hawaii [Wolfe et al., 2003, Merz et al., 2019]. Deeper seismicity associated with volcano eruption has also been reported in La Palma [Torres-González et al., 2020], with event

magnitudes ranging from 0.9 to 2.7 and a depth range of 12 to 33 km, which is comparable to what is observed offshore of Mayotte.

The occurrence of such an intense upward migrating seismicity along with the birth of a new volcano clearly indicate that the earthquakes are caused by a deep magma transfer offshore Mayotte. This sequence is striking for the occurrence of several events of relatively large magnitude ($M_w \geq 5$), which is uncommon in an area formerly considered to be a moderately seismic region. To further analyze the relationship between earthquakes and the migrating magma, our moment tensor estimates are discussed in the next two sections.

4. Moment tensor solutions consistent with regional stresses

Moment tensor solutions together with centroid depth, station coverage, and the percentage of CLVD, ISO and DC components are listed in Figures 2 and 3. For each earthquake, deviatoric moment tensor (DMT), full moment tensor (FMT) and double couple (DC) solutions are depicted in red, gray and blue, respectively. DMT and FMT solutions are very similar for most earthquakes, with only minor differences. Some shallow events are associated with large non-DC components, hence with significant differences between DC and moment tensor solutions (i.e., FMT and DMT). This is evidenced in the Hudson diagram [Hudson et al., 1989] presented in Figure 4(a), showing that several earthquakes have a non-negligible CLVD and ISO components. The origin of such large non-DC components is discussed in Section 5.

The dominant strike-slip regime is obvious: almost all earthquakes present a right-lateral strike-slip focal mechanism with a relatively consistent strike angle. This is also visible in Figure 4(b), with P and T axes showing NE–SW extension and NW–SE compression, which is similar to the GCMT catalog and Cesca et al. [2020]. Even earthquakes with a large non-DC component are consistent with this orientation of the principal axes. This observation is in good agreement with regional GNSS observations in the region of the Comoros archipelago [Stamps et al., 2018, Lemoine et al., 2020]. Using a combined stress inversion of focal mechanisms, deformation structures and intrusions, Famin et al. [2020] found that the Comoros archipelago experiences a dextral shear deformation with maximum compressive horizontal stress in the NW–SE direction and NE–SW extension. More locally, earthquakes offshore eastern Mayotte are located beneath a volcanic ridge that exhibits multiple NE–SW extensional features consistent with the direction of our T-axes [Feuillet et al., 2021].

VT earthquakes are generally considered to be brittle ruptures within the volcanic edifice triggered by stress perturbations induced by magma activity. However, different relationships have been observed between VT earthquakes and magma intrusions. In particular, Roman and Cashman [2006] showed that basaltic volcanoes are often associated with migrating earthquakes ahead of the dike tip with focal mechanism P-axes parallel to the regional maximum compressive stress [i.e., dike propagation model; Ukawa and Tsukahara, 1996], while other sequences on strato-volcanoes depict random hypocenter distributions around inflating dikes with focal mechanisms presenting P-axes rotated ~90° from the maximum compressive regional stress [i.e., dike inflation model; Roman, 2005]. These differences are likely related to a number of factors including the existence of pre-existing faults in the vicinity of the dike, the regional stress-field and the properties of the ascending magma.

Observations at the onset of the Mayotte volcano-seismic crisis with migrating seismicity associated with focal mechanisms parallel to regional stresses are more consistent with the dike propagation model proposed by Ukawa and Tsukahara [1996]. The observation of basanitic pillow lava flows following the eruption [reported by Feuillet et al., 2021] thus confirms the idea that VT seismicity at Mayotte reflect stress changes induced by dike propagation. Moreover, given their large magnitudes ($M_w \geq 5.0$), the earthquakes observed at the onset of the sequence probably do not correspond to ruptures of previously intact rocks and rather occur on pre-existing faults that are already loaded by regional stresses. This agrees with stress calculations of Rubin and Gillard [1998], showing that VT events larger than magnitude 1.0 likely occur on pre-existing structures already close to failure. This is also confirmed by observations on volcanoes indicating that earthquakes triggered by dike migration usually occur on pre-existing fault systems [Gargani et al., 2006, Lengliné et al., 2016, Duputel et al., 2019].

5. Non-DC component of shallow earthquakes

As pointed out in the previous section, several VT earthquakes are associated with a large non-DC component during the Mayotte sequence (see Figures 2–4). As shown in Figure 5(a), most of earthquakes with large non-DC components (>50%) correspond to events shallower than 15 km. We do not observe any correlation of non-DC components with the event magnitudes. Similar non-DC components have also been reported by Cesca et al. [2020]. To assess the impact of such large non-DC component on waveform fits, we evaluate the ratio of RMS misfits computed for the FMT and DC solutions. Results shown in Figure 5(b) indicate a relatively moderate
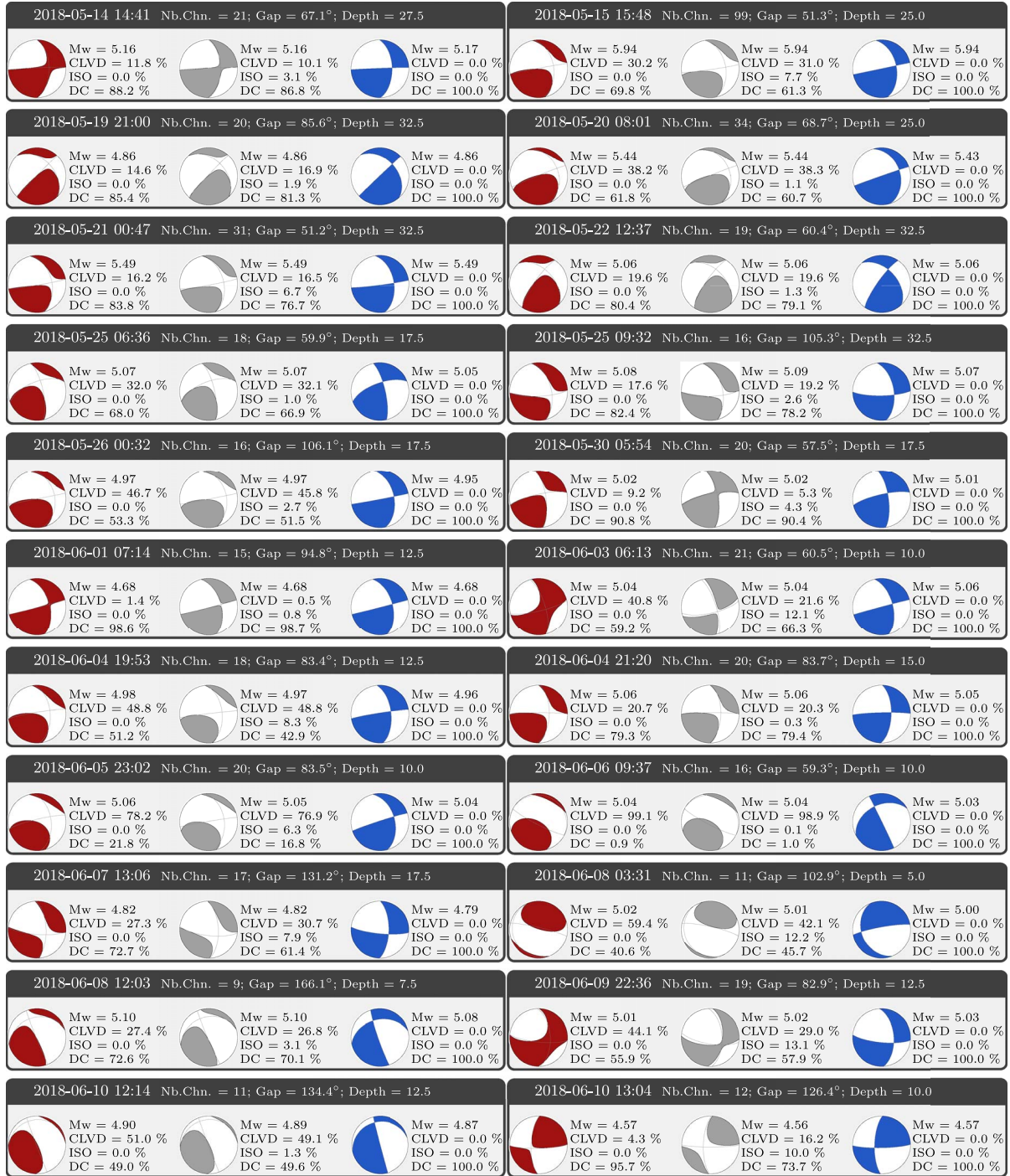
Figure 2. Moment tensor solutions for the events analyzed in this study. In red, gray and blue are the beachball obtained from the deviatoric moment tensor (DMT), full moment tensor (FMT), and double couple (DC) inversion, respectively. For each earthquake we present the number of channels, the azimuthal gap of the station coverage, depth and the beachball along with the corresponding CLVD, ISO and DC percentage.
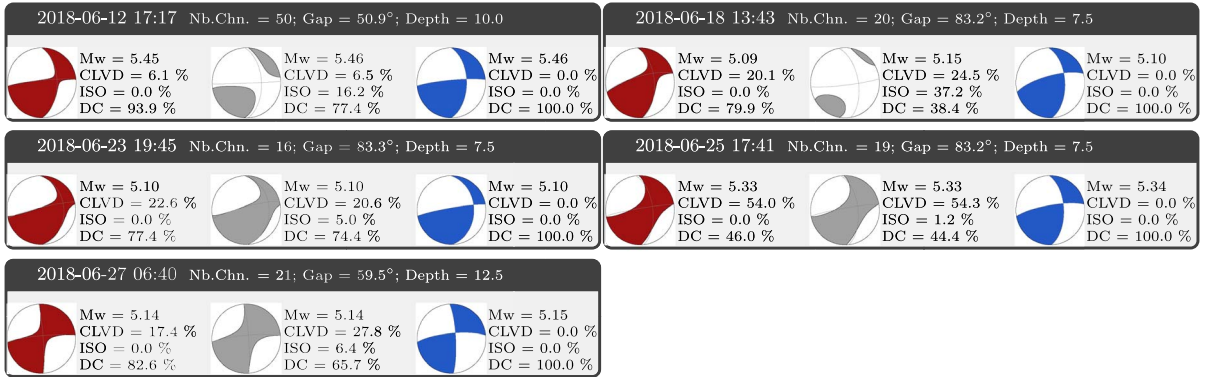
Figure 3. Moment tensor solutions for the events analyzed in this study. In red, gray and blue are the beachball obtained from the deviatoric moment tensor (DMT), full moment tensor (FMT), and double couple (DC) inversion, respectively. For each earthquake we present the number of channels, the azimuthal gap of the station coverage, depth and the beachball along with the corresponding CLVD, ISO and DC percentage.
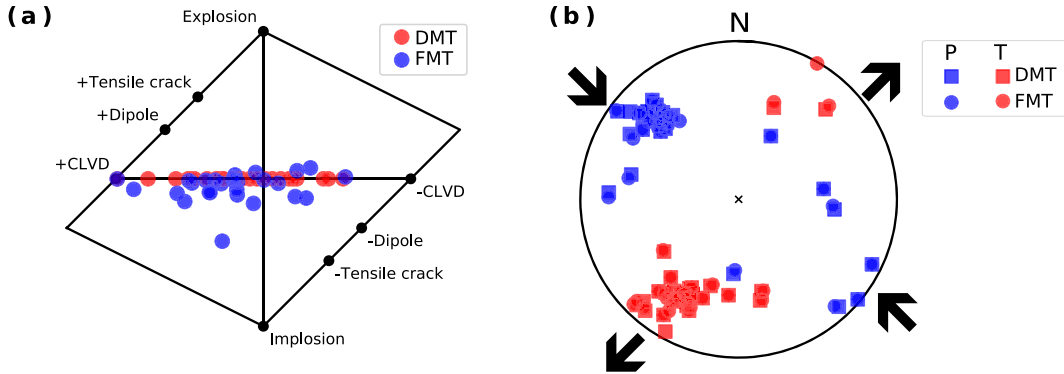

Figure 4. Hudson diagram and tension and pressure axis for each earthquake. (a) Hudson diagram Hudson et al. [1989]. Blue and red indicate inversion solutions for FMT and DMT, respectively. (b) Pressure axes (P) are represented in blue. Tension (T) axes are represented in red. Circles and square indicate inversion solutions for FMT and DMT, respectively.

overall reduction of data misfit when inverting for the full moment tensor (i.e., FMT) compared to a DC parametrization. Here, we recall that FMT and DC solutions are inverted independently (i.e., DC parameters are not estimated by decomposing the FMT solution). Unsurprisingly, the reduction of data misfit increases as a function of the non-DC percentage, showing that a DC source cannot fit data as well as a FMT solution for earthquakes with a large non-DC component. This is illustrated in Figure 6 showing the waveform fit of FMT and DC solutions for the earthquake with the largest non-DC component (event ID 2018-06-05 T23:02 in Figure 2). FMT and DMT

solutions being very similar for this earthquake, we only show synthetics of the FMT solution. The deterioration of waveform fit for the DC solution is visible at multiple stations (see ABPO, FOMA, LODK and ATD in Figure 6).

Different factors could explain the large non-DC component of earthquakes: one possibility could be crack opening/closure related to volcanic activity (e.g., caldera collapse, dike inflation/deflation, perturbation of magma circulation, etc.). Another possibility could be related to mismodeling of a complex source with a single point source model. Large non-DC components related to dike inflation/deflation
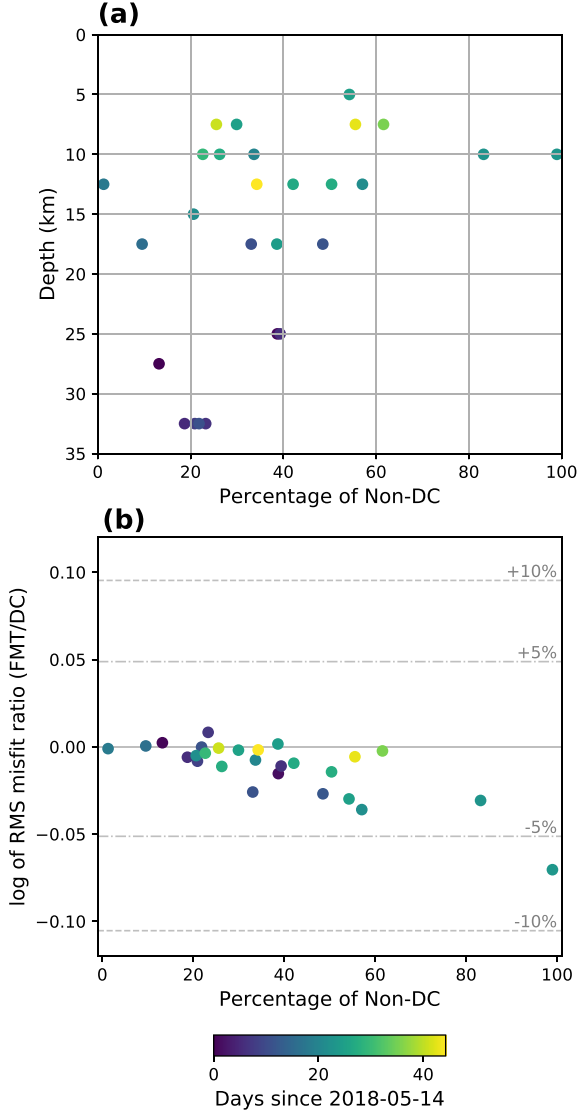
Figure 5. Percentage of non-DC components compared to the depth of the events and waveform misfit. (a) Percentage of non-DC as a function of the depth of the events obtained by a full moment tensor inversion. (b) The logarithm of the root means square (RMS) waveform misfit ratio between the solutions obtained with the full moment tensor and the double couple inversion. The colors indicate the days since 2018-05-14.

have been previously reported in Iceland [Hrubcová et al., 2021] for smaller magnitude VT earthquakes ($1 < M \leq 4$). Rodríguez-Cardozo et al. [2021] reported

230 VT earthquakes from $3.7 \leq M_w < 5.5$ and depths between 1–8 km, some of them with considerable non-DC components in the collapse of the Bárðarbunga caldera, Iceland. In particular, they observed that the CLVD component increases with the magnitude, relating it to slip on a curved fault and to the caldera collapse.

However, given the moderate magnitude of earthquakes that we investigate, and the long-period waveforms used in the inversion, the effect of source complexity seems quite unlikely to be the origin of misfit. Finally, there is the possibility of a spurious origin (e.g., contamination by ambient noise or inaccuracies in the Earth model).

In the following, we explore the possibility that the non-DC events observed offshore Mayotte could correspond to the combination of strike-slip motion and dike opening/closing associated with magma propagation. From the equations provided by Dufumier and Rivera [1997, appendix A], we write the surface area of an opening crack as:

$$S = \frac{3M_2^D}{2\mu\Delta u} \tag{5}$$

where M_2^D is the second largest eigenvalue of the deviatoric moment tensor (i.e., $M_2^D = M_2 - (M_1 + M_2 + M_3)/3$, μ is the shear modulus, and Δu is the opening of the dike. If we assume a square dike of characteristic length L, we can write

$$L = \sqrt{\frac{3M_2^D}{2\mu\Delta u}}. \tag{6}$$

Assuming that magma is migrating within the opening/closing dike at the timescale of the earthquake source duration, we estimate the average velocity of the migrating magma as:

$$V = \sqrt{\frac{3M_2^D}{2\mu\Delta u T_r^2}} \tag{7}$$

where T_r is the source duration. We can also estimate the magma flow rate F as:

$$F = V L\Delta u \tag{8}$$

$$F = \frac{3M_2^D}{2\mu T_r}. \tag{9}$$

We then estimate the average magma propagation velocity for each event to evaluate if the non-DC component could be related to fluid transport. We consider dike widths (Δu) ranging from 0.5 m
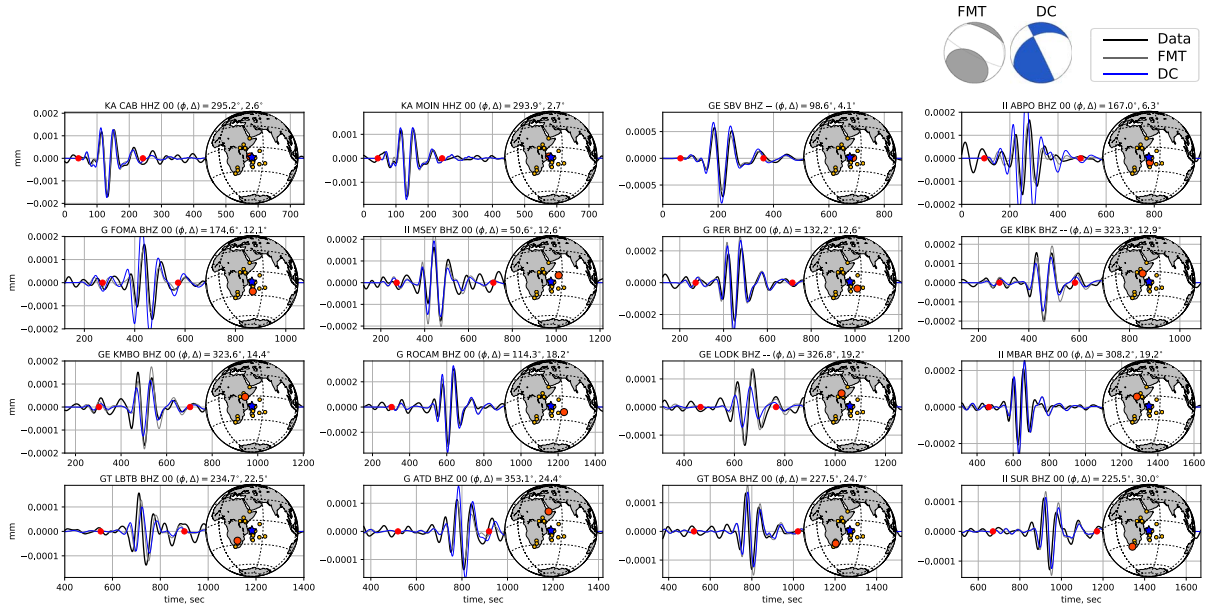
Figure 6. Waveform fit for event 2018-06-06 09:37. Observations (black) are compared with predictions created using the same centroid location but different moment tensor solutions. Gray and blue lines correspond to synthetics computed using the full moment tensor (FMT) and double couple (DC) solutions represented at the top of the figure, respectively.

to 10 m. The former value corresponds to a width typically observed on basaltic volcanoes, and the latter is an extremely large value to get a lower bound estimate of the velocity [Rubin, 1995]. For the FMT solutions obtained in this study, we estimate source duration assuming $T_r = 2t_s$, where t_s is the time-shift between the origin time and the centroid time. Centroid time-shift has been proven to provide reliable rupture duration estimates that are less affected by long tails in moment rate functions and by arbitrary modeling choices [Duputel et al., 2013, Meier et al., 2017]. For solutions provided by Cesca et al. [2020], we assume the scaling relation $T_r = 0.6 \times 10^{-8} \, M_0^{1/3}$ [Duputel et al., 2012] since no centroid times are inverted for this catalog. Figure 7 shows the magma migration velocities estimated using (7) with both the Cesca et al. [2020] catalog and our solutions. Estimated velocities range from 44 m/s to 1565 m/s and from 9.9 m/s to 350 m/s for dike openings of 0.5 m and 10 m, respectively. Even considering dike opening of 10 m, most non-DC events are associated with unreasonably large magma migration speeds greater than 100 m/s. For comparison, a rough estimate of the upward migration speed of earthquakes suggest

that the dike propagated at an average velocity of 0.05 m/s between 2018/05/19 and 2018/06/08 (see Supplementary Figure 2). To remove any dependency on the dike width, we also estimate the magma flow rate in Figure 8 using (9). The estimated flow rates are globally much larger than the average flow rate of 180 m³·s⁻¹ estimated by Feuillet et al. [2021].

Shallow moderate magnitude ($M \geq 5$) events with significant non-DC components have been previously observed around active volcanoes. Such earthquakes have been associated with caldera collapses driven by pressure variations in magma reservoirs [e.g., Ekström, 1994, Shuler et al., 2013, Duputel et al., 2019], migration of hydrothermal fluids, perturbation of magma and circulation of gases through shallow conduits [e.g., Chouet and Matoza, 2013], resonance of the fluids [e.g., Maeda and Kumagai, 2017] or complexities in the source [e.g., curved fault slip Rodríguez-Cardozo et al., 2021]. During caldera collapse events, we expect to have many focal mechanisms with vertical T or P axes [Shuler et al., 2013, Duputel and Rivera, 2019]. Even if strike-slip earthquakes occasionally occur on ring fault systems [cf., Rodríguez-Cardozo et al., 2021], there is currently no
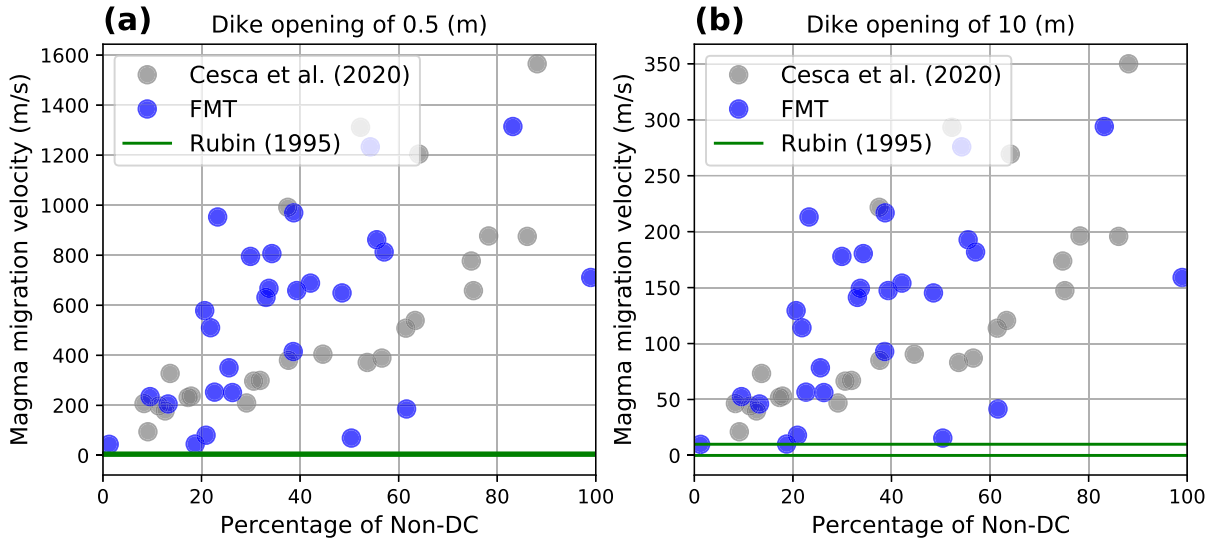
Figure 7. Magma migration velocity of the fluid as a function of the non-DC percentage. Gray and blue circles represent the solutions obtained by Cesca et al. [2020] and the present study, respectively. Green lines correspond a propagation velocities for mantle-derived dikes 0.01 and 10 m/s [Rubin, 1995]. We consider dike widths (Δu) of 0.5 m (a) and 10 m (b).
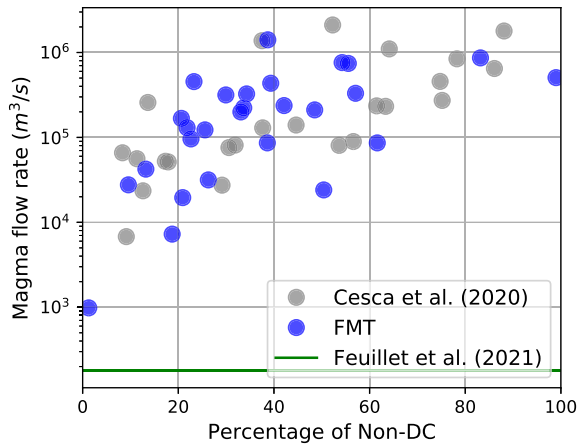

Figure 8. Magma flow rate as a function of the non-DC percentage. Gray and blue circles represent the solutions obtained by [Cesca et al., 2020] and the present study, respectively. Green lines correspond to the estimate magma flow rate of Mayotte eruption 180 m³/s [Feuillet et al., 2021].

indication of any caldera collapse at the location of the distal seismic swarm. There are indications of a resonating magma body (at the origin of VLP signals)

with a structure possibly outlining a caldera, but this structure is located closer to Mayotte, in the vicinity of the so-called proximal swarm [Feuillet et al., 2021, Cesca et al., 2020]. Dike resonance also appears unlikely as these phenomena are more typically associated with very long-period signals with marked peak frequencies, while earthquakes studied here have a frequency content similar to regular VT earthquakes.

As mentioned above, large non-DC components can also be associated with spurious origin such as ambient noise or inaccuracies in the Earth model [Šílený, 2009, Kumar et al., 2015]. This seems to be the case in Mayotte as DC solutions fit that data almost as well as FMT solutions (cf., Figures 5 and 6); suggesting that the studied earthquakes correspond to pure-shear ruptures. Moreover, as shown in Supplementary Figure 3, the non-DC part of moment tensors often differs between catalogs. In particular, Cesca et al. [2020] suggests positive isotropic components and negative CLVD for most events while our catalog is dominated by negative isotropic components and positive CLVD. Such variability among catalogs is consistent with bootstrapping results of Cesca et al. [2020], showing that the non-DC components are generally poorly resolved. Uncertainty in the moment tensor solutions increases at shal-

low depth [Morales-Yáñez et al., 2020, Fukao et al., 2018, Sandanbata et al., 2021]. The enhanced non-DC component of shallow earthquakes could be an artifact due to the mismodeling of the crustal structure in the source region. Depending on the velocity models, the Moho depth in the Mayotte area varies from 5 to 30 km [e.g., Coffin et al., 1986, Laske et al., 2013, Bassin et al., 2000, Pratt et al., 2017, Cesca et al., 2020]. While our 3D Earth model is based on CRUST2.0, which assumes an oceanic crust of thickness 12.5 km, Dofal et al. [2021] proposed recently that the region corresponds to a 17 km-thick continental crust overlying a magmatic underplated layer defining a second interface at a depth of ~27 km.

6. Conclusion

Characterizing the source of earthquakes off the east coast of Mayotte is essential to understand the link between magma transport and seismic faulting in the region. Consistently with other catalogs, our CMT solutions indicate an upward migration of seismic events at the onset of the Mayotte seismo-volcanic crisis. Although the region remains seismically active as of January 2022, the largest earthquakes of the sequence with magnitude $M_w \geq 5.0$ occurred during this initial phase in May–June 2018. Most earthquakes have a strike-slip mechanism in agreement with regional stresses in the Comoros archipelago. Our catalog along with solutions by Cesca et al. [2020] and GCMT include some shallow events associated with large non-DC components that could have been interpreted as opening or closing of subvertical dikes. However, our analysis indicate that these large non-DC components are probably not physical (i.e., not related to dike opening/closing) and are rather artifacts induced by mismodeling due to inaccuracies in the shallow velocity structure. The migration of earthquakes along with the consistency of focal mechanism with regional stresses suggest that seismic events are triggered by stress perturbations induced by the upward propagation of magma. Given their large magnitudes (i.e., up to $M_w = 5.9$), the triggered seismic events likely occur on pre-existing strike-slip faults already loaded by ambient stresses. This volcano-seismic sequence thus demonstrate how a magma intrusion can induce relatively large earthquakes even in a moderately seismic region.

Conflicts of interest

Dedication

The manuscript was written through contributions of all authors. All authors have given approval to the final version of the manuscript.

Acknowledgments

Supplementary data

Supporting information for this article is available on the journal's website under https://doi.org/10.5802/crgeos.150 or from the author.

References

Ágústsdóttir, T., Woods, J., Greenfield, T., Green, R. G., White, R. S., Winder, T., Brandsdóttir, B., Steinthórsson, S., and Soosalu, H. (2016). Strike-slip faulting during the 2014 Bároarbunga-holuhraun dike intrusion, central Iceland. *Geophys. Res. Lett.*, 43(4), 1495–1503.

Albuquerque Seismological Laboratory (ASL)/USGS (1988). Global Seismograph Network (GSN—IRIS/USGS). International Federation of Digital Seismograph Networks.

Albuquerque Seismological Laboratory (ASL)/USGS (1992). New China Digital Seismograph Network. International Federation of Digital Seismograph Networks.

Albuquerque Seismological Laboratory (ASL)/USGS (1993). Global Telemetered Seismograph Network (USAF/USGS). International Federation of Digital Seismograph Networks.

Audru, J.-C., Bitri, A., Desprats, J.-F., Dominique, P., Eucher, G., Hachim, S., Jossot, O., Mathon, C., Nédellec, J.-L., Sabourault, P., Sedan, O., Stollsteiner, P., and Terrier-Sedan, M. (2010). Major natural hazards in a tropical volcanic island: A review for Mayotte Island, Comoros archipelago, Indian Ocean. *Eng. Geol.*, 114(3), 364–381.

Bassin, C., Laske, G., and Masters, G. (2000). The current limits of resolution for surface wave tomography in North America. *EOS Trans. AGU*, 81, article no. F897. https://igppweb.ucsd.edu/~gabi/crust2.html.

Battaglia, J., Ferrazzini, V., Staudacher, T., Aki, K., and Cheminée, J.-L. (2005). Pre-eruptive migration of earthquakes at the Piton de la Fournaise volcano (Réunion Island). *Geophys. J. Int.*, 161(2), 549–558.

Cesca, S., Letort, J., Razafindrakoto, H. N. T., Heimann, S., Rivalta, E., Isken, M. P., Nikkhoo, M., Passarelli, L., Petersen, G. M., Cotton, F., and Dahm, T. (2020). Drainage of a deep magma reservoir near Mayotte inferred from seismicity and deformation. *Nat. Geosci.*, 13, 87–93.

Chouet, B. A. and Matoza, R. S. (2013). A multidecadal view of seismic methods for detecting precursors of magma movement and eruption. *J. Volcanol. Geotherm. Res.*, 252, 108–175.

Coffin, M. F., Rabinowitz, P. D., and Houtz, R. E. (1986). Crustal structure in the Western Somali Basin. *Geophys. J. Int.*, 86(2), 331–369.

Dofal, A., Fontaine, F., Michon, L., Barruol, G., and Tkalcic, H. (2021). Nature of the crust beneath the islands of the mozambique channel: Constraints from receiver functions. *J. Afr. Earth Sci.*, 184, article no. 104379.

Dufumier, H. and Rivera, L. (1997). On the resolution of the isotropic component in moment tensor inversion. *Geophys. J. Int.*, 131(3), 595–606.

Duputel, Z., Lengliné, O., and Ferrazzini, V. (2019). Constraining spatiotemporal characteristics of magma migration at Piton de la Fournaise volcano from pre-eruptive seismicity. *Geophys. Res. Lett.*, 46(1), 119–127.

Duputel, Z. and Rivera, L. (2019). The 2007 caldera collapse of Piton de la Fournaise volcano: Source process from very-long-period seismic signals. *Earth Planet. Sci. Lett.*, 527, article no. 115786.

Duputel, Z., Rivera, L., Kanamori, H., and Hayes, G. (2012). W phase source inversion for moderate to large earthquakes (1990–2010). *Geophys. J. Int.*, 189(2), 1125–1147.

Duputel, Z., Tsai, V. C., Rivera, L., and Kanamori, H. (2013). Using centroid time-delays to characterize source durations and identify earthquakes with unique characteristics. *Earth Planet. Sci. Lett.*, 374, 92–100. https://www.sciencedirect.com/science/article/pii/S0012821X13002690.

Dziewonski, A. M., Chou, T.-A., and Woodhouse, J. H. (1981). Determination of earthquake source parameters from waveform data for studies of global and regional seismicity. *J. Geophys. Res. Solid Earth*, 86(B4), 2825–2852.

Ekström, G. (1994). Anomalous earthquakes on volcano ring-fault structures. *Earth Planet. Sci. Lett.*, 128(3), 707–712.

Ekström, G., Nettles, M., and Dziewoński, A. (2012). The global cmt project 2004–2010: Centroid-moment tensors for 13,017 earthquakes. *Phys. Earth Planet. Inter.*, 200–201, 1–9.

Emerick, C. and Duncan, R. (1982). Age progressive volcanism in the comores archipelago, western indian ocean and implications for Somali plate tectonics. *Earth Planet. Sci. Lett.*, 60(3), 415–428.

Famin, V., Michon, L., and Bourhane, A. (2020). The comoros archipelago: a right-lateral transform boundary between the Somalia and Lwandle plates. *Tectonophysics*, 789, article no. 228539.

Feuillet, N. (2019). MAYOBS1 French Oceanographic Cruise, RV Marion Dufresne SISMER Database (French Oceanographic Fleet, 2019).

Feuillet, N., Jorry, S., Crawford, W. C., Deplus, C., Thinon, I., Jacques, E., Saurel, J. M., Lemoine, A., Paquet, F., Satriano, C., Aiken, C., Foix, O., Kowalski, P., Laurent, A., Rinnert, E., Cathalot, C., Donval, J.-P., Guyader, V., Gaillot, A., Scalabrin, C., Moreira, M., Peltier, A., Beauducel, F., Grandin, R., Ballu, V., Daniel, R., Pelleau, P., Gomez, J., Besançon, S., Geli, L., Bernard, P., Bachelery, P., Fouquet, Y., Bertil, D., Lemarchand, A., and Van der Woerd, J. (2021). Birth of a large volcanic edifice offshore Mayotte

via lithosphere-scale dyke intrusion. *Nat. Geosci.*, 14, 787–795.

Fukao, Y., Sandanbata, O., Sugioka, H., Ito, A., Shiobara, A., Watada, S., and Satake, K. (2018). Mechanism of the 2015 volcanic tsunami earthquake near Torishima, Japan. *Sci. Adv.*, 4(4), article no. eaao0219.

Gargani, J., Geoffroy, L., Gac, S., and Cravoisier, S. (2006). Fault slip and coulomb stress variations around a pressured magma reservoir: consequences on seismicity and magma intrusion. *Terra Nova*, 18(6), 403–411.

GEOFON Data Centre (1993). GEOFON Seismic Network. Deutsches GeoForschungsZentrum GFZ.

Hrubcová, P., Doubravová, J., and Vavryčuk, V. (2021). Non-double-couple earthquakes in 2017 swarm in reykjanes peninsula, sw iceland: Sensitive indicator of volcano-tectonic movements at slow-spreading rift. *Earth Planet. Sci. Lett.*, 563, article no. 116875.

Hudson, J. A., Pearce, R. G., and Rogers, R. M. (1989). Source type plot for inversion of the moment tensor. *J. Geophys. Res. Solid Earth*, 94(B1), 765–774.

Institut de Physique du Globe de Paris (IPGP) (2006). Karthala Volcano Monitoring Network (Karthala).

Institut de Physique du Globe de Paris (IPGP) and Ecole et Observatoire des Sciences de la Terre de Strasbourg (EOST) (1982). GEOSCOPE, French Global Network of broad band seismic stations.

Komatitsch, D., Vilotte, J.-P., Tromp, J., Afanasiev, M., Bozdag, E., Charles, J., Chen, M., Goddeke, D., Hjorleifsdottir, V., Labarta, J., Le Goff, N., Le Loher, P., Liu, Q., Maggi, A., Martin, R., McRitchie, D., Messmer, P., Michea, D., Nissen-Meyer, T., Peter, D., Rietmann, M., de Andrade, S., Savage, B., Schuberth, B., Siemenski, A., Strand, L., Tape, C., Xie, Z., and Zhu, H. (2015). SPECFEM3D GLOBE v7.0.0 [software]. Computational Infrastructure for Geodynamics. https://geodynamics.org/cig/software/specfem3d_globe/.

Kumar, R., Gupta, S., and Kumar, A. (2015). Non-double-couple mechanism of moderate earthquakes occurred in lower siang region of Arunachal Himalaya: Evidence of factors affecting non-DC. *J. Asian Earth Sci.*, 98, 105–115.

Laske, G., Masters, G., Ma, Z., and Pasyanos, M. (2013). Update on crust1. 0—a 1-degree global model of Earth's crust. In *Abstract EGU2013-2658 presented at 2013 Geophysical Research Abstracts*,

volume 15, page 2658.

Lemoine, A., Briole, P., Bertil, D., Roullé, A., Foumelis, M., Thinon, I., Raucoules, D., de Michele, M., Valty, P., and Hoste Colomer, R. (2020). The 2018–2019 seismo-volcanic crisis east of Mayotte, Comoros islands: seismicity and ground deformation markers of an exceptional submarine eruption. *Geophys. J. Int.*, 223(1), 22–44.

Lengliné, O., Duputel, Z., and Ferrazzini, V. (2016). Uncovering the hidden signature of a magmatic recharge at Piton de la Fournaise volcano using small earthquakes. *Geophys. Res. Lett.*, 43(9), 4255–4262.

Lengliné, O., Duputel, Z., and Okubo, P. G. (2021). Tracking dike propagation leading to the 2018 Kīlauea eruption. *Earth Planet. Sci. Lett.*, 553, article no. 116653.

Maeda, Y. and Kumagai, H. (2017). A generalized equation for the resonance frequencies of a fluid-filled crack. *Geophys. J. Int.*, 209(1), 192–201.

MedNet Project Partner Institutions (1990). Mediterranean Very Broadband Seismographic Network (MedNet).

Meier, M.-A., Ampuero, J., and Heaton, T. H. (2017). The hidden simplicity of subduction megathrust earthquakes. *Science*, 357(6357), 1277–1281.

Merz, D. K., Caplan-Auerbach, J., and Thurber, C. H. (2019). Seismicity and velocity structure of Lō'ihi submarine volcano and southeastern Hawai'i. *J. Geophys. Res. Solid Earth*, 124(11), 11380–11393.

Michon, L. (2016). The volcanism of the comoros archipelago integrated at a regional scale. In Bachelery, P., Lenat, J.-F., Di Muro, A., and Michon, L., editors, *Active Volcanoes of the Southwest Indian Ocean*, page 481. Springer-Verlag, Berlin, Heidelberg.

Morales-Yáñez, C., Duputel, Z., and Rivera, L. (2020). Impact of 3-D Earth structure on W-phase CMT parameters. *Geophys. J. Int.*, 223(2), 1432–1445.

Neal, C. A., Brantley, S. R., Antolik, L., Babb, J. L., Burgess, M., Calles, K., Cappos, M., Chang, J. C., Conway, S., Desmither, L., Dotray, P., Elias, T., Fukunaga, P., Fuke, S., Johanson, I. A., Kamibayashi, K., Kauahikaua, J., Lee, R. L., Pekalib, S., Miklius, A., Million, W., Moniz, C. J., Nadeau, P. A., Okubo, P., Parcheta, C., Patrick, M. R., Shiro, B., Swanson, D. A., Tollett, W., Trusdell, F., Younger, E. F., Zoeller, M. H., Montgomery-Brown, E. K., Anderson, K. R.,

Poland, M. P., Ball, J. L., Bard, J., Coombs, M., Dietterich, H. R., Kern, C., Thelen, W. A., Cervelli, P. F., Orr, T., Houghton, B. F., Gansecki, C., Hazlett, R., Lundgren, P., Diefenbach, A. K., Lerner, A. H., Waite, G., Kelly, P., Clor, L., Werner, C., Mulliken, K., Fisher, G., and Damby, D. (2019). The 2018 rift eruption and summit collapse of Kilauea Volcano. *Science*, 363(6425), 367–374.

Nougier, J., Cantagrel, J., and Karche, J. (1983). The Comores archipelago in the western Indian Ocean: volcanology, geochronology and geodynamic setting. *J. Afr. Earth Sci.*, 5(2), 135–145.

Nyblade, A. (2017). Broadband seismic experiment in NE Uganda to investigate plume-lithosphere interactions (NE Uganda) [Data set]. International Federation of Digital Seismograph Networks.

Pratt, M. J., Wysession, M. E., Aleqabi, G., Wiens, D. A., Nyblade, A. A., Shore, P., Rambolamanana, G., Andriampenomanana, F., Rakotondraibe, T., Tucker, R. D., Barruol, G., and Rindraharisaona, E. (2017). Shear velocity structure of the crust and upper mantle of Madagascar derived from surface wave tomography. *Earth Planet. Sci. Lett.*, 458, 405–417.

RESIF (1962). RESIF-RLBP French Broad-band network, RESIF-RAP strong motion network and other seismic stations in metropolitan France.

RESIF (2018). CEA/DASE broad-band permanent network in metropolitan France.

REVOSIMA/IPGP (2019). Bulletin de l'activité sismovolcanique á Mayotte. Bulletin n°1 du 1 au 31 juillet 2019. http://www.ipgp.fr/sites/default/files/ipgp_1er_bulletin_info_sismo_volcanique_mayotte-cor.pdf.

REVOSIMA/IPGP (2021). Bulletin de l'activité sismovolcanique á Mayotte. Bulletin n°37 du 1er au 31 décembre 2021. http://www.ipgp.fr/sites/default/files/ipgp_revosima_n37_20220106.pdf.

Ritsema, J., Deuss, A., van Heijst, H. J., and Woodhouse, J. H. (2011). S40rts: a degree-40 shear-velocity model for the mantle from new rayleigh wave dispersion, teleseismic traveltime and normal-mode splitting function measurements. *Geophys. J. Int.*, 184(3), 1223–1236.

Rodríguez-Cardozo, F., Hjörleifsdóttir, V., Jónsdóttir, K., Iglesias, A., Franco, S. I., Geirsson, H., Trujillo-Castrillón, N., and Hensch, M. (2021). The 2014–2015 complex collapse of the bárðarbunga caldera, iceland, revealed by seismic moment tensors. *J. Volcanol. Geotherm. Res.*, 416, article no. 107275. https://www.sciencedirect.com/science/article/pii/S0377027321001049.

Roman, D. C. (2005). Numerical models of volcanotectonic earthquake triggering on non-ideally oriented faults. *Geophys. Res. Lett.*, 32(2), article no. L02304.

Roman, D. C. and Cashman, K. V. (2006). The origin of volcano-tectonic earthquake swarms. *Geology*, 34(6), 457–460.

Rubin, A. M. (1995). Propagation of magma-filled cracks. *Annu. Rev. Earth Planet. Sci.*, 23(1), 287–336.

Rubin, A. M. and Gillard, D. (1998). Dike-induced earthquakes: Theoretical considerations. *J. Geophys. Res. Solid Earth*, 103(B5), 10017–10030.

Sandanbata, O., Kanamori, H., Rivera, L., Zhan, Z., Watada, S., and Satake, K. (2021). Moment Tensors of Ring-Faulting at Active Volcanoes: Insights Into Vertical-CLVD Earthquakes at the Sierra Negra Caldera, Galápagos Islands. *J. Geophys. Res. Solid Earth*, 126(6), article no. e2021JB021693.

Saurel, J.-M., Jacques, E., Aiken, C., Lemoine, A., Retailleau, L., Lavayssière, A., Foix, O., Dofal, A., Laurent, A., Mercury, N., Crawford, W., Lemarchand, A., Daniel, R., Pelleau, P., Bès de Berc, M., Dectot, G., Bertil, D., Roullé, A., Broucke, C., Colombain, A., Jund, H., Besançon, S., Guyavarch, P., Kowalski, P., Roudaut, M., Apprioual, R., Battaglia, J., Bodihar, S., Boissier, P., Bouin, M. P., Brunet, C., Canjamale, K., Catherine, P., Desfete, N., Doubre, C., Dretzen, R., Dumouche, T., Fernagu, P., Ferrazzini, V., Fontaine, F. R., Gaillot, A., Géli, L., Griot, C., Grunberg, M., Guzel, E. C., Hoste-Colomer, R., Lambotte, S., Lauret, F., Léger, F., Maros, E., Peltier, A., Vergne, J., Satriano, C., Tronel, F., Van der Woerd, J., Fouquet, Y., Jorry, S. J., Rinnert, E., Thinon, I., and Feuillet, N. (2022). Mayotte seismic crisis: building knowledge in near real-time by combining land and ocean-bottom seismometers, first results. *Geophys. J. Int.*, 228(2), 1281–1293.

Scripps Institution of Oceanography (1986). Global seismograph network (GSN—IRIS/USGS). International Federation of Digital Seismograph Networks.

Shuler, A., Nettles, M., and Ekström, G. (2013). Global observation of vertical-CLVD earthquakes at active volcanoes. *J. Geophys. Res. Solid Earth*, 118(1), 138–164.

Sigmundsson, F., Hooper, A., Hreinsdóttir, S.,

Vogfjörd, K. S., Ófeigsson, B. G., Heimisson, E. R., Dumont, S., Parks, M., Spaans, K., Gudmundsson, G. B., Drouin, V., Árnadóttir, T., Jónsdóttir, K., Gudmundsson, M. T., Högnadóttir, T., Fridriksdóttir, H. M., Hensch, M., Einarsson, P., Magnússon, E., Samsonov, S., Brandsdóttir, B., White, R. S., Ágústsdóttir, T., Greenfield, T., Green, R. G., Hjartardóttir, A. R., Pedersen, R., Bennett, R. A., Geirsson, H., La Femina, P. C., Björnsson, H., Pálsson, F., Sturkell, E., Bean, C. J., Möllhoff, M., Braiden, A. K., and Eibl, E. P. S. (2015). Segmented lateral dyke growth in a rifting event at Bároarbunga volcanic system, Iceland. *Nature*, 517, 191–195.

Šílený, J. (2009). Resolution of non-double-couple mechanisms: simulation of hypocenter mislocation and velocity structure mismodeling. *Bull. Seismol. Soc. Am.*, 99(4), 2265–2272.

Stamps, D. S., Saria, E., and Kreemer, C. (2018). A geodetic strain rate model for the East African rift system. *Sci. Rep.*, 8, article no. 732.

Torres-González, P., Luengo-Oroz, N., Lamolda, H., D'Alessandro, W., Albert, H., Iribarren, I., Moure-García, D., and Soler, V. (2020). Unrest signals after 46 years of quiescence at Cumbre Vieja, La Palma, Canary Islands. *J. Volcanol. Geotherm. Res.*, 392, article no. 106757. https://www.sciencedirect.com/science/article/pii/S037702731930366X.

Ukawa, M. and Tsukahara, H. (1996). Earthquake swarms and dike intrusions off the east coast of Izu Peninsula, central Japan. *Tectonophysics*, 253(3), 285–303.

Utrecht University (UU Netherlands) (1983). NARS [Data set]. International Federation of Digital Seismograph Networks.

Vavryčuk, V. (2015). Moment tensor decompositions revisited. *J. Seismol.*, 19, 231–252.

Wolfe, C. J., Okubo, P. G., and Shearer, P. M. (2003). Mantle fault zone beneath Kilauea volcano, Hawaii. *Science*, 300(5618), 478–480.

Zinke, J., Reijmer, J., Thomassin, B., Dullo, W.-C., Grootes, P., and Erlenkeuser, H. (2003). Postglacial flooding history of Mayotte lagoon (Comoro Archipelago, southwest Indian Ocean). *Mar. Geol.*, 194(3), 181–196.